Flank instability on Mount Etna: radon, radar interferometry and geodetic data from the south-western boundary of the unstable sector

Marco Neri[(1)]*, Francesco Guglielmino[(1)] and Derek Rust[(2)]

[1]Istituto Nazionale di Geofisica e Vulcanologia, Sezione di Catania, Piazza Roma 2, 95123 - Catania, Italy.

neri@ct.ingv.it, guglielmino@ct.ingv.it,

[2]Department of Geography and Earth Sciences, Brunel University; Uxbridge, UB8 3PH, U.K.

derek.rust@brunel.ac.uk

Running title: Flank instability on Mount Etna

***Corresponding author :**

Marco Neri
Istituto Nazionale di Geofisica e Vulcanologia
Sezione di Catania
Piazza Roma, 2 – 95123 CATANIA - ITALY
Tel. ++39.095.7165861
Fax. ++39.095.435801
e-mail: neri@ct.ingv.it

Citation:

Neri, M., F. Guglielmino, and D. Rust (2007), Flank instability on Mount Etna: Radon, radar interferometry, and geodetic data from the southwestern boundary of the unstable sector, J. Geophys. Res., 112, B04410, doi:10.1029/2006JB0047

Journal of Geophysical Research - Solid Earth

Abstract
Understanding Etnean flank instability is hampered by uncertainties over its western boundary. Accordingly, we combine soil radon emission, InSAR and EDM data to study the Ragalna fault system (RFS) on the SW flank of the volcano. Valuable synergy developed between our differing techniques, producing consistent results and serving as a model for other studies of partly obscured active faults. The RFS, limited in its surface expression, is revealed as a complex interlinked structure ~14 km long that extends from the edifice base towards the area of summit rifting, possibly linking north-eastwards to the Pernicana fault system (PFS) to define the unstable sector. Short-term deformation rates on the RFS from InSAR data reach ~7 mm a^{-1} in the satellite line of sight on the upslope segment and ~5 mm a^{-1} on the prominent central segment. While combining this with EDM data confirms the central segment of the RFS as a dextral transtensive structure, with strike-slip and dip-slip components of ~3.4 and ~3.7 mm a^{-1} respectively. We measured thoron (^{220}Rn, half-life 56 secs) as well as radon and, probably because of its limited diffusion range, this appears a more sensitive but previously unexploited isotope for pinpointing active near-surface faults. Contrasting activity of the PFS and RFS reinforces proposals that the instability they bound is divided into at least three sub-sectors by intervening faults, while, in section, fault-associated basal detachments also form a nested pattern. Complex temporal and spatial movement interactions are expected between these structural components of the unstable sector.

Keywords: Multidisciplinary study; Ragalna fault system; radon and thoron; InSAR; EDM; volcano collapse models

1. Introduction
Since the well known eruption of Mt St Helens in 1980 volcanic edifices have been increasingly recognised as inherently unstable constructions prone to structural failure, most notably involving large scale catastrophic flank collapse in ocean island volcanoes such as those of the Hawaiian and Canary chains. Instability is driven by combinations of gravity, magma pressure, lack of buttressing support, presence of an underlying weak substrate to the edifice, increasing pore pressure associated with volcanism, dyke emplacement, tectonic uplift and faulting (Siebert 1984; McGuire, 1996; Merle and Borgia, 1996; Voight and Elsworth, 1997; Tibaldi, 2001; Acocella and Neri, 2003, 2005; Neri et al., 2005; Falsaperla et al., 2006; Acocella et al., 2006). Mount Etna, because it is one of the most intensively monitored and studied volcanoes in the world, offers the promise of developing a better understanding of this instability and the factors that drive it. However, although large scale flank movement on Etna has become increasingly accepted since it was first proposed in 1992 (Borgia et al 1992; Lo Giudice and Rasà, 1992), basic questions remain, notably on the areal extent, nature, rate and future development of the instability. Our purpose in the present paper is to address these questions using new multidisciplinary data (radon-thoron emission from soil, radar interferometry and geodetic), from the relatively unstudied Ragalna fault system (RFS) that is thought to form the western boundary of Etnean flank instability (Rust and Neri, 1996; Rust et al., 2005).

2. Geological background
Mount Etna, situated on the eastern coast of Sicily (Figure 1), is more than 3300 m high, about 38-45 km in diameter, and has arisen rapidly from a succession of overlapping central vents in approximately the last 200 Ka (Romano, 1982; Calvari et al., 1994;

Coltelli et al., 1994; Corsaro et al., 2002; Branca et al., 2004; and references therein), after an earlier (commencing ~500 ka) phase of fissure style volcanism (Romano, 1982). The northern and western parts of the volcano overlie and are buttressed against a pre-existing topography developed in metamorphic and sedimentary rocks within a southward verging system of thrusted nappes, the Apennine-Maghrebian Chain, at the southern margin of the Eurasian plate. By contrast, the southern and eastern flanks of the edifice overlie marine early Quaternary plastic clays that accumulated in the foredeep created on the tectonically depressed northern margin of the northward-dipping downgoing African plate (Lentini, 1982).

This tectonic regime imposes overall north-south compression to the Etnean region (Lanzafame et al., 1997a), and field relationships between the Apennine-Maghrebian Chain rocks and sub Etnean clays indicate that thrusting continued until at least mid-Pleistocene times (Lanzafame et al., 1997b). Active regional uplift is indicated by outcrops of the early Quaternary marine clays that occur up to several hundred metres above sea level (asl) on the volcano flanks, and by Holocene reefs that are being uplifted at a rate of about 2 mm a^{-1} along the Etnean coast (Firth et al., 1996; Rust and Kershaw, 2000).

This compressional framework is transected by a number of seismogenic structures of regional tectonic importance. Of these the largest is the Malta Escarpment, a structure that strikes NNW-SSE and defines the eastern and southeastern edge of the Sicilian continental shelf, marking the boundary with the oceanic-affinity crust of the Ionian Sea to the east. Dip-slip displacement on the Malta Escarpment amounts to some 3 km (Hirn et al., 1997), and where it intersects the coast of Sicily on the eastern side of Mount Etna it is represented by a series of active faults (the Timpe fault system; Figure 1) with scarps up to 200 m and fault planes displaying both dip-slip and right-oblique-slip kinematic indicators (Lanzafame et al., 1996; Monaco et al., 1997; Corsaro et al., 2002).

3. Edifice instability

Since the early 1990s numerous studies have proposed large scale sliding of the eastern and southern sectors of the volcano (Neri et al., 1991; Borgia et al., 1992; Lo Giudice and Rasà 1992; Rust and Neri, 1996; Garduño et al., 1997; Borgia et al. 2000a, b; Froger et al., 2001; Acocella et al., 2003; Neri et al., 2004), and recently of the western flank too (Lundgren et al., 2004). The base level of the sliding sector has been inferred to lie at 1-2 km asl (Bousquet and Lanzafame, 2001), at 0-1 km asl (Lo Giudice and Rasà, 1992), at ~6 km below sea level (bsl) (Borgia et al., 1992) and at both shallow and deep levels (Tibaldi and Groppelli, 2002; Rust et al., 2005). These studies coincide in placing the northern boundary of instability at the E-W trending PFS (Figure 1; Acocella and Neri, 2005). There has been, however, less agreement on the southern and western boundaries, with different authors emphasizing the role and importance of the NW-SE trending Mascalucia -Trecastagni fault system (MTFS in Figure 1; Lo Giudice and Rasà 1992; Froger et al., 2001; Azzaro, 2004) and the N-S trending RFS (Figure 1; Rust and Neri, 1996; Lundgren and Rose, 2003; Lundgren et al., 2004). More recent proposals emphasize the complexity of the unstable sector, suggesting it is divided into three main blocks characterized by different movement rates and directions separated by the RFS, the MTFS and the S.Venerina fault system (SV in Figure 1; Acocella et al., 2003; Burton et al., 2004; Neri et al., 2004), and that the instability operates at different scales and time frames and is nested both with depth and in map view (Rust et al., 2005). Such models are well supported by numerous studies that, using different methods, identify instability of a wide sector on the eastern, southern (Borgia et al., 2000b; Froger et al., 2001;

Lundgren et al., 2003; Bonforte and Puglisi, 2003; Puglisi and Bonforte, 2004) and western (Lundgren et al., 2004) flanks of the volcano.

3.1. Ragalna fault system

Three distinct fault segments are clearly visible near Ragalna, one N–S striking and 4.5 km long, and two shorter segments striking SW–NE but several kilometres apart and with opposing senses of downthrow (Figures 1 and 2A). The relationship between these segments is unclear and, in the field there is no apparent continuity either upslope towards the summit area of the volcano or downslope towards the base of the edifice (Figure 1).

By comparison, the PFS is recognised as the northern margin of instability with some 20 km of faulting continuity (Neri et al., 2004) and a clear linkage to the volcano summit via the NE Rift (Neri et al, 1991; Acocella and Neri, 2005; Neri et al., 2005; Walter et al., 2005).

In 1996 Rust and Neri proposed that the Ragalna fault segments formed a continuous structure via a transfer zone occupied by series of recently active cinder cones, and should be regarded as a fault system comparable to the PFS. Moreover, fresh appearing fault scarps up to 20 m high, offsets of very late Pleistocene and Holocene volcanic sequences (Figure 2A), deflected stream courses and disrupted cultural features at fault crossings, as well as an en echelon series of open fractures led them to suggest the RFS was an active right oblique structure with a minimum long-term dip-slip component of about 1.4 mm a^{-1}. Also noted were the consistent left-stepping arrangement of the axes of an en echelon series of late Pleistocene – early Holocene lava domes, mapped by Romano (1979) and Rasà et al. (1982), and their close spatial association with the faulting (Figure 2A). This relationship suggested a relatively long-standing role in accommodating right-lateral displacement in this part of the volcano; consistent with the subsurface expression of the faulting on their reconstruction of the sub-Etnean surface (Rust and Neri, 1996). These lines of evidence, together with seismicity patterns (see also Rust et al., 2005 for more detail on this aspect), led them to suggest that the RFS should be regarded as the main western boundary of active flank instability on Etna. However a number of important questions remain and the present paper seeks to address these. First, the possibility of a continuation from the distinctive delta shaped upslope termination of the surface faulting, where the junction of two fault segments creates a triangular horst (Figure 2A). Identifying the RFS as forming a boundary to flank instability implies that there must be continuity upslope to the summit area, ultimately linking with the NE Rift and the PFS to complete the boundary between stable and unstable parts of the edifice.

A second specific question to be addressed by the present study is the possible downslope continuity of the RFS. The surface expression of the faulting indicates gradually diminishing offset as it apparently ends at a small and relatively degraded cinder cone on the lower flank of the volcano (Rust and Neri, 1996). However, the RFS probably forms the boundary to a relatively deep (~5 km) detachment surface that daylights beyond the edifice (Borgia et al, 1992; Rust and Neri, 1996; Borgia et al, 2000b; Rust et al, 2005) and this implies that the faulting, although possibly obscured by agricultural activity and with limited offset as the termination of an essentially rotational instability is approached, must extend farther south.

A further specific question concerns the structural arrangement in the transfer zone occupied by the cinder cones and, more generally, the present work seeks to better document the activity level, nature and geodynamic role of the RFS.

4. Methodology

4.1. Radon and thoron measurements

^{222}Rn is a short-lived decay product derived from ^{238}U, a ubiquitous element in volcanic rocks. Radon is a noble gas, chemically inert and one of the most dense gases known. It also has a short half-life of 3.8 days. Together, these characteristics intrinsically limit its diffusivity, with studies indicating limits of approximately 2 m in soils and 2 mm in waters (Dubois et al., 1995; Conner et al., 1996), and with a diffusion coefficient of only 0.12 cm^2 s^{-1} (Tanner, 1964). As a result, superficial anomalies in radon emissions rely on the convective flow of gases that facilitate the transport of radon from greater depth within soils and radon emissions can be used as dynamic tracers for soil degassing (Shapiro et al., 1982; Toutain et al., 1992; Heinicke et al., 1992; Toutain and Baubron, 1999). Active faults are likely to have a higher permeability than surrounding structures and therefore, in combination with degassing of CO_2 from depth, near-surface faults are likely to be locations of high soil degassing and therefore elevated radon concentrations (Abdoh and Pilkington, 1989; Ciotoli et al., 1999; Baubron et al., 2002; Tansi et al., 2005). In volcanic areas deep emanations of CO_2 from magma can produce strong degassing through soils at the surface (Allard et al., 1991). These facts have led to radon surveys being carried out on several volcanoes in order to determine the location and activity of near-surface faults (Crenshaw et al., 1982; Aubert and Baubron, 1988; Baubron et al., 1990, 1991; Burton et al., 2004; Alparone et al., 2005).

We used the Durridge RAD7 instrument to measure radon concentrations in soils (Figure 3A). This instrument uses a pump with a 1 litre minute $^{-1}$ flow rate to extract soil gases into an internal accumulation chamber where electrostatic collection of alpha-emitters and spectral analysis takes place that precisely measures the energy of every particle detected. Alpha emissions with an energy of 6.002 MeV, for example, are attributable to decay of the ^{218}Po daughter product and allow ^{222}Rn activity to be recorded rapidly in units of Bq m^{-3}. The instrument also measures alpha emission from the ^{216}Po daughter (half-life 150 ms), produced by ^{220}Rn decay. This radon isotope, known as thoron, has a half life of 56 s and is produced within a decay chain starting from ^{232}Th.

4.2. Radar interferometry: SAR image selection and InSAR processing

In order to analyze the Ragalna structures, radar images taken over Mt. Etna by the ERS-1 and ERS-2 satellite were selected, processed and analyzed. All the images used for this study are shown in Table 1. The choice of suitable pairs was based on two criteria: firstly, to obtain pairs that had the minimum perpendicular baseline component available (to minimize geometrical decorrelation) and, second, to obtain orbit pairs with different time windows and epochs in order to provide good coverage of the time span 1993-2002. The data set is composed of ascending (frame 747; 23:16 local time) orbit data and were processed to zero compensated Doppler, slant range projection, phase-preserved single look complex image (SLC) images.

The procedure used for the generation of interferometric outputs relevant to the selected image pairs was the so called "*two pass interferometry*" (Massonnet and Feigl, 1998). This method requires two SAR images to generate a real phase interferogram that is correlated with topography and changes in topography. To analyze topographic displacements, the topography-dependant part of the interferogram is eliminated using an independent DEM. The height values are then converted into synthetic phase-values before the phase-values of the real and synthetic interferogram are subtracted from each

other. In this way residual phase-values are obtained, resulting in a differential interferogram that is uniquely correlated to variations in topography.
To co-register the two images and calculate the interferometric geometry we used the precise orbits of the ERS satellites produced at the Delft Institute for Earth Oriented Space Research (DEOS). The interferogram was projected onto an orthogonal geographic coordinate system so that users avoid working in the distorted radar geometry.
Since the phase difference of the image pair corresponds to the change in the round-trip path length of radar waves to ground targets, an interferogram is similar to a contour map of the change in distance to the ground surface along the Line of the Sight (LOS) of the satellite. Each contour line, or fringe, represents 28 mm, i.e. half the wavelength of the ERS radar.

4.3. Geodetic measurements

In March 1999 six geodetic stations were established in a tight network spanning about 350 m of the south central part of the N-S-striking fault segment within the RFS. The stations were reoccupied using the same equipment (factory recalibrated), and the same procedures, in November 2005. Three of the original six stations had been lost through human disturbance since the original survey but, fortunately, the remaining stations span the fault and provide two lines suitably orientated to assess dip-slip and strike-slip components of movement (Table 2 and Figure 2B).

Each station consisted of a steel survey nail driven into bedrock lava outcrops or, in two cases, into concrete foundations. Distances between stations were measured using a Sokkia SET3C Electronic Total Station instrument (Serial number 106926) equipped with a digital readout precise to 1 mm. The SET3C EDM (electronic distance measurement) instrument uses an infrared light beam to rapidly calculate the distance to a reflecting prism. The instrument was mounted on a Sokkia EDM tripod using an adjustable base plate that allowed accurate levelling and centring vertically above each survey nail using built-in bubble levels and an optical plumb. Indexing was also done to ensure accurate measurement of angles (readout precise to 1 second of arc), with the instrument automatically providing horizontal distances converted from measured angular distances (Figure 3B). A duplicate tripod and base plate combination was used for the EDM reflector, a Sokkisha single prism type with a similar plumb, positioned at the next station in the network. To eliminate any errors in set up all measurements were repeated after rotating the instrument 180^{o} about both vertical and horizontal axes.

5. Results

5.1. Radon and thoron fluxes

We have carried out measurements over a wide area on Mount Etna since 1998 and these have shown strong radon emissions from active faults, with radon activities reaching ~10,000-26,000 Bq m^{-3} (Burton et al., 2004). Other measurements were carried out close to the Etna summit craters, where radon emissions were negligible, apart from the Torre del Filosofo area at 2920 m where up to 15,000 Bq m^{-3} of radon was observed (Alparone et al., 2005). Measurements in non-active areas produced very low radon activities of ~300 Bq m^{-3}.
Field survey of the RFS was concentrated in the 5-8 July 2005 period and sampling of some reference points was repeated regularly in order to maintain quality control of the measurements. This control demonstrated a variability of less than 20% (average ~9%)

over the survey period. Forty six radon measurements were obtained from five transects distributed both in the well known N-S-striking central segment of the RFS (profile C-C') and in the areas where the presence of the fault is only suspected (profiles A-A', B-B', D-D' and E-E', see Figure 4 for locations). As far as possible the profiles were run in a direction orthogonal to the faults, with one measurement every 100-200 metres.
In the northern area, where Rust and Neri (1996) hypothesised a connection from the RFS to the S Rift and the summit craters (Figure 1), two profiles (A-A' and B-B', 1.56 and 2.4 km long respectively) were completed (Figure 4), with values of ~5,000 (^{222}Rn) and ~21,000 (^{220}Rn) Bqm^{-3} recorded in their central areas. The box in the top left corner in Figure 4 shows a contour map of radon ^{222}Rn (A) distribution, where a NE-SW 500-700 m-wide linear radon anomaly is evident, straddling the presumed extension of the fault.
Along the central segment of the RFS, the C-C' profile (1.2 km long; Figure 4) shows an increase in thoron emission (^{220}Rn up to 25,400 Bq m^{-3}) in comparison to the northern measurements described above. The highest value is reached a few tens of metres west of the fault, which is here characterized by marked open fractures and a ~4 m high scarp.
The ~2.5 km long D-D' profile is located in the suggested transfer zone connecting the central and southern segments of the RFS (Figure 4), where no ground fractures and/or fault scarps are visible.
Here the highest values of radon (^{222}Rn = 4,000-5,000 Bq m^{-3}) occur near-symmetrically a few hundred metres on either side of the supposed fault plane. However, a high value for thoron (^{220}Rn = 51,300 Bq m^{-3}) was found exactly along the supposed southern projection of the central N-S fault segment.
Concerning the possible southern continuation of the RFS the 1.6 km-long E-E' profile showed the highest values recorded during this field work (^{222}Rn up to 18,750Bq m^{-3} and ^{220}Rn up to 61,600 Bq m^{-3}; Figure 4). However, although there is a marked and coincident peak in both radon and thoron, the pattern also includes ascending values at the western end of the profile. Here the profile reaches the margin of the S. Maria di Licodia community, where urbanisation hampers locating suitable open ground to extend the transect and further investigate the apparent radon anomaly beneath the town.

5.2. Radar interferometry

The interferograms used in this study cover the time interval from 21 November 1993 to 9 October 2002 (Figure 8). This interval is divided into four partially overlapping periods in order to determine the distribution, timing and nature of movement on the RFS. In this interval volcanic activity was characterized by: i. quiet degassing from the summit vents (until mid-1995); ii. progressively more intense and frequent reactivation of the four summit craters (from mid-1995 to mid-2001; Harris and Neri, 2002; Calvari et al, 2003; Behncke et al., 2003; 2006); and iii. two flank eruptions in July-August 2001 and October 2002-January 2003 (Allard et al., 2006 and references therein). After the interval recorded by InSAR, in September 2004-March 2005, a third flank eruption also occurred (Burton et al., 2005; Neri and Acocella, 2006).
The interferogram in frame "A" of Figure 6 (21 November 1993 – 30 September 1997) shows a clear N-S aligned discontinuity corresponding to the central segment of the RFS (yellow line C) and resulting from a visible relative shift up to ~3/4 fringe. A northern continuation of this discontinuity is also clearly visible (broken pink line NC), marking the possible existence of a northern prosecution of the central fault, as previously suggested by Lundgren et al., 2004. The proposed continuation of the NE-SW-striking northern segment of RFS (broken white line NE), which connects the fault system with the summit area, is slightly less evident in this interferogram compared to the N-S fault; seeming to

disappear close to the top of the volcano (~2,800 m asl), where the poor coherence (e.g., due to the seasonally intermittent snow cover) of the interferogram limits our analysis. Movement on the known southern segment (yellow line S in Figure 6A) of the RFS is also clearly visible, together with the presumed connection (broken white line SW) between the central and southern segments of the RFS.
In the short period represented in frame "B" of Figure 6 (28 May 1997 – 13 May 1998) the main feature highlighted by the interferogram is movement along the central segment (C) of the RFS (a relative shift of ~1/4 fringe is visible), together with the northward continuation (NC). By contrast, no clear evidence of movement is deducible on the NE-SW segments of the RFS, either in the north (NE) or south (SW).
Frame "C" of Figure 7 covers a time interval of just over 3 years (8 January 1997 – 8 March 2000) and, once again, clear movement is visible in the central segment (C) of the RFS (with a relative shift of ~1/2 fringe). Less evident deformation is shown in the upper northeast sector (NE), while the southwest-striking segments (both S and SW) have subdued definition in the interferogram.
The last frame "D" of Figure 7 covers nearly two years (8 November 2000 – 9 October 2002). In this interferogram all the RFS displays clear movement, particularly in the northeast part of the system (NE) where there is a relative shift of ~1 fringe.

5.3. Geodetic data

The EDM geodetic results, presented in Table 2, show clear evidence for dextral transtensive movement on the central segment of the RFS between March 1999 and November 2005. All measurements are internallyconsistent, both in amount and direction, and repeat measurements agree to within no more than 3 mm over a distance of some 250 m. Over the 6.5 year re-measurement time interval the distance between Station 1 (on the west side of the fault) and Station 3 (on the east side) increased by 23-25 mm and between Station 1 and Station 4 (on the east side of the fault) the distance decreased by 25-30 mm (Figure 2 and Table 2). These distances were then corrected, using trigonometry, to compensate for the 20^{o} angular difference between the survey lines and the strike of the fault; thus giving a more accurate measure of movement parallel and normal to the fault . This correction indicates an increase of 24-27 mm normal to the fault over the time period and, bringing Station 1 and Station 4 closer together, 27-32 mm reduction in distance parallel to the fault. This correction, used in order to obtain the most useful data from the remaining geodetic stations, thus amounts to a maximum of 2 mm; very small in comparison to the total amount of movement recorded.
Kinematic indicators such as slickenlines are not preserved to help determine fault slip but trigonometry can be used to show that the 27 – 32 mm shortening parallel to the fault between Station 1 and Station 4, which we adopt as a measure of strike-slip displacement, is inadequate alone to account for the increase in distance between Station 1 and Station 3 normal to the fault. This increased distance therefore must include extension (dip-slip displacement) at the fault. Furthermore, this extension can be assumed to affect both Station 3 and Station 4 since they are on the same side of the fault (Figure 2B). Importantly, this relative eastward movement acts to *increase* the Station 1 – Station 4 distance, thus offsetting the measured shortening. Consequently, the strike-slip component of movement derived from the reduction in fault-parallel distance must be regarded as a minimum value only. At the same time, because some of the fault-normal increase is produced by strike-slip movement, this measurement represents a maximum value for extension (dip-slip component of movement). Accordingly, in terms of slip-rates and regardless of whether the angular correction is adopted or not, the distance changes indicate an average minimum rate for right-lateral

movement of 4.0 – 5.0 mm a^{-1} and, for extensional (dip-slip) movement, an average maximum rate of 3.5 – 4.0 mm a^{-1} (Table 2). These are the values used in the discussion that follows.

6. Discussion

In general the differing techniques appear to complement and strengthen each other and provide a consistent set of results that give new insights on the extent, behaviour and role of the RFS. Measurements of radon and thoron are effective in outlining areas of anomalously high gas flux in the Etnean context and, by comparing transects across known and suspected but obscured faults, the proposition that active near-surface faults act as pathways for these short-lived isotopes seems valid. Thoron, with its very short half life and consequent limited diffusion range, seems particularly useful in pinpointing faults in reasonable detail.

Although SAR interferometry also aids location of obscure faults its chief value lies in identifying and quantifying fault movements in space and time. However, interferograms fail to identify tectonic structures during those time intervals when there is no movement and therefore, for a study such as ours, need to be combined with field data. InSAR imagery, furthermore, shows only the sum of deformation effects in a certain part of the Earth's surface for a certain time interval. It is thus possible that the direction and amount of movement identified along structures is the result of different deformation factors impossible to distinguish from each other, such as volcano inflation/deflation cycles. Geodetic measurements, employ a well established technique in comparison to the other two approaches we use, and are valuable in providing tangible field evidence of movement on clearly defined structures. As described above, our results also allow us to suggest values for the rate of dip-slip movement, as well as documenting the sense and rate of the strike-slip component. Moreover, the ground-based measurements supplement and complement InSAR data because our geodetic measurements document movement on and very close to the fault itself, whereas the satellite data encompasses total deformation over a broad area.

Below we discuss in turn the three main uncertain aspects of the RFS identified at the start of this paper and, with similar reference to the stated aims of our study, the wider role of the RFS in Etnean flank instability.

6.1. The northern RFS

InSAR images show that the northward extension of the central segment of the RFS beyond its surface termination (NC in Figures 6 and 7) is clear in the long period interferograms (A,C and D) and progressively diminishes northwards. It averages a little less than 7 mm a^{-1} in the line of sight of the satellite (LOS) until disappearing close to the summit craters. This northwards disappearance of the signal may be due to diminution of movement along the fault, but it is more likely that it results from incoherent signals in proximity to the summit craters due mainly to the discontinuous presence of snow cover and typical layover and shadow geometric errors. The lack of radon anomalies along this N-S fault extension could be due to an insufficient westward extent of the two profiles made in that area; these being limited by rough terrain made up of very coarse-grained recent scoriaceous lavas. In such settings the RAD7 instrument does not effectively record radon values because the percentage of cavities in the regolith (>0.5 dm^3) is too high, resulting in the instrument measuring essentially atmospheric conditions at the shallow depth of 50 cm sampled by the probe.

The continuation of the RFS towards the summit craters is clearly visible in radon profiles A-A' and B-B' (Figure 4). The radon anomaly extends in a NE-SW sense with a width of

about 500-700 m, leaving little doubt about the effective continuation of this fault towards the NE, beyond the morphologically visible segment that terminates at about 1200 m elevation (Figure 4). In the same zone, the connection between the RFS and the summit area through a NE-SW fault is only visible on interferogram D, where the movement is ~14 mm a^{-1} in LOS (NE in Figure 10). However, this may result from the combination of different types of deformation, including the general inflation of the volcano (Lundgren et al., 2003, Bonforte and Puglisi, 2003; Puglisi and Bonforte, 2004) and the faulting associated with the opening of the 2001 eruptive fissure (Billi et al., 2003; Lanzafame et al., 2003; Acocella and Neri, 2003). The fact that no movement along this portion of the fault system is visible in other interferograms may result from either, the objective difficulty in analyzing a zone close to the summit area or, from the absence of significant movement in the preceding time interval (1993-2000). On the other hand, the dynamics of the south-eastern sector of Etna affected by spreading shows an increasing deformation trend only from 2001 onwards (Neri et al., 2004, 2005; Rust et al., 2005; Walter et al., 2005; Allard et al., 2006), which seems to support the second possibility.

6.2. The central RFS

In the central portion of the RFS, where the fault is marked by a prominent scarp up to 10 m high, the ground-based EDM measurements document right-lateral transtensive displacement since 1999 at rates of at least 4 - 5 mm a^{-1} for the strike-slip component and a maximum of 3.5 - 4 mm a^{-1} for the extensional component. But the two remeasured EDM lines are insufficient to directly determine the exact vector of fault movement. However, the InSAR data in the longer time-period interferograms (A, C and D) show movement on this segment of the RFS of between ½ and ¾ fringe. Allowing for a typical error of ~¼ fringe, these InSAR values average 4.7±1.8 mm a^{-1} in LOS (Figures 6 and 7).The LOS unit look vector is defined by “ViewEast”, “ViewNorth”, “ViewVert”, which are, respectively for the Ragalna area: 0.360, 0.078, -0.929. To calculate the LOS displacement we use the following:

$$LOS=(\Delta_x * \mathit{ViewEast})+(\Delta_y * \mathit{ViewNorth})+(\Delta_z * \mathit{ViewVert})$$

where Δ_x, Δ_y, Δ_z are the 3D components of the displacement.

In the field the fault scarp is nearly vertical, so we can assume that the extension measured by EDM is due mainly to the dip-slip component of displacement. Consequently, assuming a Δ_z component of -3.7 mm a^{-1} (corresponding to ~90% of the E-W extension measured by EDM), we recalculate the east-west and north-south components of movement on the fault, obtaining the following values:

$\Delta_{x=}$+1.5 mm a^{-1} (East-West)
$\Delta_{y=}$-3.4 mm a^{-1} (North-South)

Therefore, the LOS value is:

$$LOS=(1.5 * 0.360)+(-3.4 * 0.078)+(-3.7 * -0.929) = 3.7 \text{ mm } a^{-1}$$

This value is within the range of error of the InSAR data and it confirms a dextral transtensive movement affecting the structure. In this part of the RFS the profiles for radon (^{222}Rn) and thoron (^{220}Rn) correspond well with each other, although with thoron displaying a greater amplitude between peaks and troughs (Profile C-C’ in Figure 4).

Both profiles show peaks at the fault scarp itself but, interestingly, there are secondary peaks to the east and west that do not correspond to any mapped surface fault trace. Fractures can be seen at the ground surface in this area and it may be that shear is more distributed here. Farther south the linkage between the central and southern segments of the RFS (broken white line between C and S in Figures 6 and 7) is evident in all interferograms. In this area, high thoron values (^{220}Rn up to 51,300 Bq m^{-3}) indicate the probable position of the main fault (profile D-D' in Figure 4). In contrast, radon shows the highest values laterally, and in a nearly symmetrical position with respect to the assumed fault plane. This might be due to the structural complexity of the transfer zone between the two segments of the fault system (from N-S to NE-SW), and perhaps reflects a northward continuation of the NE-SW-striking fault segment.

6.3. The southern RFS

The SW segment of the RFS (SW in Figures 6 and 7) is visible in the two longer period interferograms (A and C). The calculated movement is 3.5 mm a^{-1} in LOS, lower than the previously described segments. However, this area falls on the margin of the InSAR imagery coverage, and the discrepancy could reflect reduced accuracy in measurements of movement.

The radon values in this area are among the highest measured along the RFS. Significant peaks in radon and thoron are evident in the central part of profile E-E' (Figure 4), corresponding to the hypothetical south-westward continuation of the fault, and with the movement recognized in interferograms A and C. However, the strong increase in radon at the western end of this profile (where the S. Maria di Licodia urban cover begins) cannot be easily interpreted. Such high values (^{222}Rn up to 18,750Bq m^{-3} and ^{220}Rn up to 61,600 Bq m^{-3}) stand out in comparison with the local background values and point to the possible existence of another active fault, possibly parallel to the known fault (NE-SW), but which cannot be mapped due to insufficient available data (see question mark in Figure 8). Such a fault, possibly inactive during the period of InSAR coverage, may also help in accounting for the disparity in slip rates identified at the beginning of this section.

6.4. The RFS and Etnean edifice instability

The multidisciplinary approach adopted in our study has greatly expanded available data on the geometry, continuity and displacement of the RFS. Foremost, is the evident connection between the various faults, striking NE-SW and N-S, that make up the RFS. The physical continuity at the surface is evident only at one point (at 1200 m elevation), where two faults form an acute angular junction (Figure 1). Other connections are unrecognizable at the surface, either through fault scarps or ground fracturing. However, both the InSAR imagery and the radon measurements shed light on connections between segments of the fault system, as well as confirming a northward continuation of the N-S central fault segment (recently highlighted by Lundgren et al., 2004) that extends onto the western flank of the volcano to at least 1650 m elevation, and a NE-SW-striking continuation towards the summit area of the volcano (broken white line in Figures 4, 6 and 7).

This newly discovered complex geometry of the RFS and the evident inter-relationships of movement between the single faults that constitute the system highlight the significance of the RFS in the geodynamic context of Mount Etna. This important fault system, which extends from the summit area to the SW margin of the volcano, has a total length exceeding 14 km.

During the period of analysis, the flanks of Etna were affected by inflation/deflation movements (Lundgren et al., 2003), and these could play a role in the RFS deformation. In detail, after the 1991-1993 eruption, edifice deflation occurred (Massonnet et al., 1995; Bonaccorso et al., 2004). In 1994, rapid inflation began and, since 1996, a gradual increase in flank instability has taken place, with displacement of the eastern and southeastern flanks (Froger et al., 2001). These events could indicate new magma supply to a central magma chamber beneath the Etnean summit at about 5 km bsl, triggering flank spreading (Lundgren et al., 2003, 2004). This process culminated in an acceleration of flank movements accompanying the 2001, 2002-2003 and 2004-2005 flank eruptions, with spreading affecting mainly the eastern and southern flanks of the volcano (Allard et al., 2006 and reference therein). Lundgren et al. (2004) and Lundgren and Rosen (2004) also detected spreading on the W flank, previously considered stable, through their analysis of InSar images. Their interpretation is not confirmed by faults clearly visible in the field and no evidence of linked deformation (such as compression at the base of the supposed west spreading sector) were detected. If spreading does affect the western flank, it is likely to be very minor and short lived, probably triggered by dyke injection, in contrast to the general spreading affecting the eastern and southern flanks of Etna, as Lundgren and Rosen (2004) suggest.

Therefore, considering all the available data, we observe that the geometry and rates of movement of the RFS are consistent with its role as the western boundary of the very large unstable sector of the volcano (Figure 8; see also Rust and Neri, 1996; Froger et al., 2001; Rust et al., 2005; Allard et al., 2006). This interpretation is also consistent with the analogue experiments conducted by Merle and Borgia in 1996.

Additionally, our study confirms the much lower rates of movement on this boundary compared to the northern margin of the unstable sector, represented by the PFS (Figure 1). In recent years, in fact, the PFS has shown extremely high deformation rates (1 - >100 cm a^{-1}; Acocella and Neri, 2005). Such variation reinforces proposals that Etnean flank instability is characterised by a complex pattern of behaviour involving structures such as the S. Venerina faults and the Mascalucia-Trecastagni fault system (Figure 1) that subdivide the unstable sector into at least three subsectors in map view (Figure 8, right panel. Neri et al., 2004, 2005; Neri and Acocella, 2006), while associated basal detachments create a movement complex that is also nested in section (Rust et al., 2005). Consequently, although the Pernicana and Ragalna systems can be ultimately linked in defining the extent of flank instability on Etna, the structural complexities of the intervening unstable sector greatly influence interactions between the two bounding systems. The high deformation rates on the PFS, for example, appear to be dissipated amongst these structures, with deformation on the RFS occurring at lower rates and possibly activating after a lag in time (Acocella et al., 2003; Neri et al., 2004; 2005; Rust et al., 2005).

Such complex interactions can be proposed with some confidence on Etna because of the very large body of research work that now exists for this volcano. This behaviour may also serve as a model for other, less well studied, volcanoes.

7. Conclusions

Our multi-pronged approach to a better understanding of the extent, activity level and geodynamic role of the Ragalna fault system (RFS) demonstrates, incidentally, a valuable synergy between the three techniques employed. The techniques strengthen and complement each other, together producing a consistent body of data and illustrating the

usefulness and applicability of the approach in studying other partially obscured but active fault systems, particularly in volcanic settings.
In terms of the specified aims of our work the following conclusions can be highlighted. The RFS is revealed as a complex interlinked structure with continuity over a distance exceeding 14 km, most notably including extensions northwards (recently proposed by Lundgren et al., 2004) from the conspicuous delta-shaped junction that marks the end of visible faulting, and north-eastwards, towards the summit craters of Mt Etna. Linkage is confirmed in a previously proposed transfer zone (Rust and Neri 1996) between two segments of the RFS separated at the surface by some 2 km. In a downslope direction continuity of the RFS is suggested as far as the transition between Etnean volcanic products and the surrounding non-volcanic bedrock.
Deformation rates during the analysis period on the RFS derived from InSAR reach a maximum of a little less than 7 mm a-1 in LOS on the upslope segment and about 5 mm a^{-1} in LOS on the central. Combining this one-dimensional value with our EDM measurements confirms the central segment of the RFS as a dextral transtensive structure, with strike-slip and dip-slip components of ~3.4 and ~3.7 mm a^{-1} respectively. The longest visible fault segment in the RFS, N-S-striking, is shown to move most constantly, while the other segments have more variable movement histories and rates. This complex deformation pattern could be due to the superimposition of inflation/deflation movements induced by the dynamics a sub-volcanic reservoir, and flank instability phenomena which affect the eastern to southern Etna flanks.
Our multidisciplinary study reinforces proposals (Rust and Neri, 1996) that the RFS is the western boundary of long term flank instability on Mt Etna and probably, via rifting in the summit craters area, links across to the Pernicana fault system that forms the northern boundary, thus encircling the unstable flank sector (Figure 8). A comparison of activity for these two fault systems suggests that the unstable sector is divided into at least three sub-sectors by intervening faults, while, in section, basal detachments associated with faults also form a nested pattern. Complex movement interactions in space and time are expected to take place between these structural components of the unstable sector.

Acknowledgments

This work was funded by grants from the Istituto Nazionale di Geofisica e Vulcanologia (INGV) and from the Dipartimento per la Protezione Civile (Italy), project V3_6/28-Etna. Many thanks go to Paul Allen, Matthew Bailey, Alex Ciocanel, David Walton and Christopher Weller for assistance with EDM measurements. Olivier Merle, Paul Lundgren and anonymous reviewer helped to improve the quality of this paper. We are grateful to John C. Mutter for the editorial handling of the paper.

References

Abdoh, A. and M. Pilkington (1989), Radon emanation studies of the Ile Bizard Fault, Montreal. *Geoexploration, 25,* 341-354.

Acocella, V. (2005), Modes of sector collapse of volcanic cones: insights from analogue experiments. *J. Geoph. Res., 110,* B02205, doi:10.1029/2004JB003166.

Acocella, V., and M. Neri (2003), What makes flank eruptions? The 2001 Etna eruption and its possible triggering mechanisms. *Bull. Volcanol. 65,* 517-529.

Acocella, V., and M. Neri (2005), Structural features of an active strike-slip fault on the sliding flank of Mt. Etna (Italy). *J. Structural Geology, 27*(2)*,* 343-355, doi:10.1016/j.jsg.2004.07.006.

Acocella, V., B. Behncke, M. Neri and S. D'Amico, S. (2003), Link between major flank slip and eruptions at Mt. Etna (Italy). *J. Geophys. Res., 30,* 2286, doi:10.1029/2003GL018642.

Acocella V., M. Neri and P. Scarlato (2006), Shallow magma emplacement during the 2002-2003 Stromboli (Italy) eruption. *Geophys. Res. Lett.*, 33, L17310, doi:10.1029/2006GL026862.

Allard P., J. Carbonnelle, D. Dajlevic, J. Lebronec, P. Morel, M.C. Robe, J.M. Maurenas, R. Faivrepierret, D. Martin, J.C. Sabroux and P. Zettwoog (1991), Eruptive and diffuse emissions of CO_2 from Mount Etna, *Nature*, 351, 387-391.

Allard P., B. Behncke, S. D'Amico, M. Neri and S. Gambino (2006), Mount Etna 1993-2005: Anatomy of an Evolving Eruptive Cycle. *Earth-Science Rev.*, 78, 85-114, doi:10.1016/j.earscirev.2006.04.002.

Alparone S., B. Behncke, S. Giammanco, M. Neri and E. Privitera (2005), Paroxysmal summit activity at Mt. Etna monitored through continuous soil radon measurements. *Geophys. Res. Lett., 32,* L16307, doi:10.1029/2005GL023352.

Aubert, M., and J.C. Baubron (1998), Identification of a hidden thermal fissure in a volcanic terrain using a combination of hydrothermal convection indicators and soil atmospheres analysis, *J. Volcanol. Geotherm. Res., 35*, 217–225.

Azzaro, R. (2004), Seismicity and active tectonics in the Etna region: constraints for a seismotectonic model. In *Etna Volcano Laboratory, Geophys. Monogr. Ser.,* vol. 143, edited by A. Bonaccorso et al., pp. 205-220, AGU, Washington, D.C.

Baubron, J.C., P. Allard and J.P. Toutain (1990), Diffuse volcanic emissions of carbon dioxide from Vulcano Island, Italy, *Nature, 344*, 51–53, 1990.

Baubron, J.C., P. Allard, J.C. Sabroux, D. Tedesco and J.P. Toutain (1991), Soil gas emanations as precursory indicators of volcanic eruption, *J. Geol. Soc. London, 148,* 571–576.

Baubron, J.C., A. Rigo and J.P.Toutain (2002), Soil gas profiles as a tool to characterise active tectonic areas: the Jaut Pass example (Pyrenees, France). *Earth and Plan. Sci. Letts. 196,* 69-81.

Behncke, B., and M. Neri (2003a), The July-August 2001 eruption of Mt. Etna (Sicily). Bull. Volcanol., 65, 461-476. doi: 10.1007/s00445-003-0274-1

Behncke, B., and M. Neri (2003b), Cycles and trends in the recent eruptive behaviour of Mount Etna (Italy), *Can. J. Earth Sci., 40,* 1405-1411, doi: 10.1139/E03-052.

Behncke, B., M. Neri and R. Carniel (2003), An exceptional case of lava dome growth spawning pyroclastic avalanches at Mt. Etna (Italy): the 1999 Bocca Nuova eruption. *J. Volcanol. Geotherm. Res.*, 124/1-2, 115-128.

Behncke, B., M. Neri and A. Nagay (2005), Lava flow hazard at Mount Etna (Italy): New data from a GIS-based study, in *Kinematics and dynamics of lava flows* edited by M. Manga and G. Ventura, *Spec. Pap. Geol. Soc. Am., 396-13,* 187-205, doi: 710.1130/2005.2396(13).

Behncke B., M. Neri, E. Pecora, V. Zanon (2006), The exceptional activity and growth of the Southeast Crater, Mount Etna (Italy), between 1996 and 2001. *Bull. Volcanol.*, 69, 149-173, doi: 10.1007/s00445-006-0061-x.

Billi, A., V. Acocella, R. Funiciello, G. Giordano, G. Lanzafame, M. Neri (2003), Mechanisms for ground-surface fracturing and incipient slope failure associated to the July-August 2001 eruption of Mt. Etna, Italy: analysis of ephemeral field data. *J. Volcanol. Geotherm. Res.*, 122, 3-4, 281-294.

Bonaccorso, A., O. Campisi, G. Falzone, S. Gambino (2004), Continuous tilt monitoring: a lesson from 20 years experience at Mt. Etna. In *Etna Volcano Laboratory, Geophys. Monogr. Ser.,* vol. 143, edited by A. Bonaccorso et al., 143, pp. 307-320.

Bonforte, A., and G. Puglisi (2003), Magma uprising and flank dynamics on Mount Etna volcano, studied using GPS data (1994–1995), *J. Geophys. Res., 108* (B3), 2153, doi:10.1029/2002JB001845.

Borgia, A., L. Ferrari and G. Pasquale (1992), Importance of gravitational spreading in the tectonic and volcanic evolution of Mount Etna. *Nature, 357*, 231-235.

Borgia, A., P.T. Delaney, R.P. Denlinger (2000a), Spreading volcanoes. A*nn. Rev. Earth Planet. Sci. 28,* 539-570.

Borgia, A., R. Lanari, E. Sansosti, M. Tesauro, P. Berardino, G. Fornaro, M. Neri and J.B. Murray (2000b), Actively growing anticlines beneath Catania from the distal motion of Mount Etna's decollment measured by SAR interferometry and GPS. *Geophys. Res. Letts., 27*, 3409-3412.

Bousquet, J.C., and G. Lanzafame (2001), Nouvelle interprétation des fractures des éruptions latérales de l'Etna: conséquences pour son cadre tectonique. *Bull. Soc. Géol. Fr., 172*, 455-467.

Branca, S., M. Coltelli and G. Groppelli (2004), Geological Evolution of Etna Volcano. In *Etna Volcano Laboratory, Geophys. Monogr. Ser.,* vol. 143, edited by A. Bonaccorso et al., pp. 49-63, AGU, Washington, D.C.

Burton M., M. Neri and D. Condarelli (2004), High spatial resolution radon measurements reveal hidden active faults on Mt. Etna, *Geophys. Res. Lett., 31*(7), L07618, doi:10.1029/2003GL019181.

Burton, M.R., M. Neri, D. Andronico, S. Branca, T. Caltabiano, S. Calvari, R.A. Corsaro, P. Del Carlo, G. Lanzafame, L. Lodato, L. Miraglia, G. Salerno and L. Spampinato (2005), Etna 2004-2005: An archetype for geodynamically-controlled effusive eruptions. *Geophys. Res. Lett., 32,* L09303, doi:10.1029/2005GL022527.

Calvari, S., G. Groppelli and G. Pasquarè (1994), Preliminary geological data on the south-western walls of Valle del Bove, Mt. Etna (Sicily). *Acta Vulcanol., 5,*15-30.

Calvari S., M. Neri and H. Pinkerton (2003), Effusion rate estimation during the 1999 summit eruption on Mt. Etna, and growth of two distinct lava flow fields. *J. Volcanol. Geotherm. Res.*, 119/1-4, 107-123.

Ciotoli, G., G. Etiope, M. Guerra, and S. Lombardi (1999), The detection of concealed faults in the Ofanto Basin using the correlation between soil-gas fracture surveys. *Tectonyphysics, 301,* 321-332.

Coltelli, M., V.H. Garduno, M. Neri, G. Pasquarè and M. Pompilio (1994) Geology of northern wall of Valle del Bove, Etna (Sicily). *Acta Vulcanol., 5,* 55-68.

Conner, C., B. Hill, P. LaFemina, M. Navarro and M. Conway (1996), Soil ^{222}Rn pulse during the initial phase of the June-August 1995 eruption of Cerro Negro, Nicaragua, *J. Volcan. Geotherm. Res., 73*, 119-127.

Corsaro, R., M. Neri and M. Pompilio (2002), Paleo-environmental and volcano-tectonic evolution of the south-eastern flank of Mt. Etna during the last 225 ka inferred from

volcanic succession of the «Timpe», Acireale, Sicily. *J. Volcanol. Geotherm. Res. 72,* 1-19

Crenshaw, W.B., S.N. Williams and R.E. Stoiber (1982), Fault location by radon and mercury detection at an active volcano in Nicaragua, *Nature, 300,* 345–346.

Dubois, C., A. Alvarez Calleja, S. Bassot and A. Chambaudet (1995), Modelling the 3-dimensional microfissure network in quartz in a thin section of granite. In *Gas Geochemistry*, edited by C. Dubois, Science Rev., pp. 357–368, Northwood.

Falsaperla S., M. Neri, E. Pecora and S. Spampinato (2006), Multidisciplinary Study of Flank Instability Phenomena at Stromboli Volcano, Italy. *Geophys. Res. Lett.*, 33, L09304, doi:10.1029/2006GL025940.

Firth, C., I. Stewart, W.M. McGuire,S. Kershaw, C. Vita-Finzi (1996), Coastal elevation changes in eastern Sicily: implications for volcano instability at Mount Etna. In *Volcano Instability on the Earth and Other Planets*, edited by W.M. McGuire, A.P. Jones and J. Neuberg, *Spec. Pub. Geol. Soc. London, 110,* 153-167.

Froger, J., O. Merle and P. Briole (2001), Active spreading and regional extension at Mount Etna imaged by SAR interferometry. *Earth Planet. Sci. Letts., 187,* 245-258.

Harris, A. J. L. and M. Neri (2002), Volumetric observations during paroxysmal eruptions at Mount Etna: pressurized drainage of a shallow chamber or pulsed supply? *J. Volcanol. Geotherm. Res.*, 116, 79-95.

Heinicke, J., G. Martinelli and U. Koch (1992), Investigation of the connection between seismicity and CO_2 - ^{222}Rn content in spring water at the Vogtland area (Germany): first results. *Abstract, XXIII General Assembly of the European Seismological Commission*, Prague.

Hirn, A., R. Nicolich, J. Gallart, M. Laigle, L. Cernobori (1997), Roots of Etna volcano in faults of great earthquakes. *Earth Planet, Sci. Letts., 148,* 171-191.

Lanzafame, G., M. Neri and D. Rust (1996), Active tectonics affecting the eastern flank of Mount Etna: structural interactions at regional and local scale, In *Etna: Fifteen years on*, edited by P.H. Gravestock and W.J. McGuire, Cheltenham and Gloucester College of Higher Education, Centre for Volcanic Research, 25-33.

Lanzafame, G., M. Neri, M. Coltelli, L. Lodato and D. Rust(1997a), North-South compression in the Mt. Etna region (Sicily): spatial and temporal distribution. *Acta Vulcanol., 9,* 121-133.

Lanzafame, G., A. Leonardi, M. Neri and D. Rust (1997b), Late overthrust of the Appenine-Maghrebian Chain at the NE periphery of Mt. Etna, Italy. *C.R. Acad. Sc. Paris, t. 324,* serie IIa, 325-332.

Lanzafame, G., M. Neri, V. Acocella, A. Billi, R. Funiciello and G. Giordano (2003), Structural features of the July-August 2001 Mount Etna eruption: evidence for a complex magmatic system. *J. Geol. Soc. Lond. 160,* 531-544.

Lentini, F. (1982), The geology of the Mt. Etna basement. *Mem. Soc. Geol. It., 23,* 7-25.

Lo Giudice, E., and R. Rasà (1992), Very shallow earthquakes and brittle deformation in active volcanic areas: the Etnean region as an example. *Tectonophysics, 202,* 257-268.

Lundgren, P., P. Berardino, M. Coltelli, G. Fornaro, R. Lanari, G. Puglisi, E. Sansosti and M. Tesauro (2003), Coupled magma chamber inflation and sector collapse slip observed with synthetic aperture radar interferometry on Mt. Etna volcano. *J. Geophys. Res. 108,* doi: 10.1029/2001JB000657.

Lundgren, P., F. Casu, M. Manzo, A. Pepe, P. Berardino, E. Sansosti, and R. Lanari (2004), Gravity and magma induced spreading of Mount Etna volcano revealed by satellite radar interferometry. *Geophys. Res. Lett.*, 31, L04602, doi: 10.1029/003GL018736.

Lundgren, P., and P. A. Rosen (2003), Source model for the 2001 flank eruption of Mt. Etna volcano, *Geophys. Res. Lett.*, 30(7), 1388, doi:10.1029/2002GL016774.

McGuire, W. J. (1996), Volcano instability: A review of contemporary themes. In *Volcano Instability on the Earth and Other Planets*, edited by W.M. McGuire, A.P. Jones and J. Neuberg, *Spec. Pub. Geol. Soc. London,* 110, 1-23.

Massonnet, D., Briole, P., Arnaud, A., 1995. Deflation of Mount Etna monitored by spaceborne radar interferometry. *Nature*, 375, 567-570.

Massonet, D. and K.L. Feigl (1998), Radar interferometry and its application to changes in the Earth's surface. *Rev. Geophys.*, 36, 441-500.

Merle, O., and A. Borgia (1996), Scaled experiments of volcanic spreading. *J. Geophys. Res., 101,* 13805-13817.

Monaco, C., P. Tapponier, L. Tortorici, P.Y. Gillot (1997), Late Quaternary slip rates on the Acireale-Piedimonte normal faults and tectonic origin of Mt. Etna (Sicily). *Earth Planet. Sci. Lett.,147,* 125-139.

Neri, M., and V. Acocella (2006), The 2004-05 Etna eruption: implications for flank deformation and structural behaviour of the volcano. *J. Volcanol. Geotherm. Res.*, 158, 195-206, doi:10.1016/j.jvolgeores.2006.04.022, .

Neri, M., V. Acocella and B. Behncke (2004), The role of the Pernicana fault system in the spreading of Mt. Etna (Italy) during the 2002-2003 eruption. *Bull. Volcanol. 66,* 417-430, doi: 10.1007/s00445-003-0322-x.

Neri, M., V. Acocella, B. Behncke, V. Maiolino, A. Ursino and R. Velardita (2005), Contrasting triggering mechanisms of the 2001 and 2002-2003 eruptions of Mount Etna (Italy). *J. Volcanol. and Geotherm. Res., 144*, 235-255, doi: 10.1016/j.jvolgeores.2004.11.025.

Neri M., B. Behncke, M. Burton, S. Giammanco, E. Pecora, E. Privitera, D. Reitano, (2006), Continuous soil radon monitoring during the July 2006 Etna eruption. Geophys. Res. Lett., 33, L24316, doi:10.1029/2006GL028394.

Neri, M., V.H. Garduño, G. Pasquarè and R. Rasà (1991), Studio strutturale e modello cinematico della Valle del Bove e del settore nord-orientale etneo. *Acta Vulcanol., 1,* 17-24.

Puglisi G. and A. Bonforte (2004), Dynamics of Mount Etna Volcano inferred from static and kinematic GPS measurements, *J. Geophys. Res., 109,* B11, B11404, doi:10.1029/2003JB002878.

Rasà, A., R. Romano and L. Lo Giudice (1982), Morphotectonic map of Mt. Etna, In *Mount Etna Volcano,* edited by *R.* Romano, *Mem. Soc. Geol. It., 23*.

Romano, R. (1979), Geological Map of Mt. Etna. CNR, Prog. Fin. Geodinamica, Istituto Internazionale di Vulcanologia, Catania, 1:50000 scale.

Romano, R. (1982), Succession of the volcanic activity in the Etnean area. *Mem. Soc. Geol. It., 23,* 27-48.

Rust, D., and M. Neri (1996), The boundaries of large-scale collapse on the flanks of Mount Etna, Sicily, In *Volcano Instability on the Earth and Other Planets*, edited by W.M. McGuire, A.P. Jones and J. Neuberg, *Spec. Pub. Geol. Soc. London,* 110, 193-208.

Rust, D., B. Behncke, M. Neri and A. Ciocanel (2005), Nested zones of instability in the Mount Etna volcanic edifice, Sicily. *J. Volcanol. and Geotherm. Res., 155*, 137-153, doi: 10.1016/j.jvolgeores.2004.11.021.

Rust, D., and S. Kershaw (2000), Holocene tectonic uplift patterns in northeastern Sicily: evidence from marine notches in coastal outcrops. *Marine Geology, 167,* 105-126.

Siebert, L. (1984) Large volcanic debris avalanches: Characteristics of source areas, deposits and associated eruptions. *J. Volcanol. Geotherm. Res., 22,* 163-197.

Shapiro, M.H., J.D. Melvin, T.A. Tombrello, J. Fong-Liang, L. Gui-Ru, M.H. Mendenhall, and A. Rice, (1982), Correlated radon and CO_2 variations near the San-Andreas fault, *Geophys. Res. Lett., 9,* 503–506.

Tanner, A. B. (1964) Radon migration in the ground: a review, In *Natural Radiation Environment,* edited by J.A.S. Adams W.M. Lowder, Univ. Chicago Press, pp.161-190, Chicago.

Tansi, C., A. Tallarico,G. Iovine, M. Folino-Gallo and G. Falcone (2005), Interpretation of radon anomalies in seismotectonic and tectonic-gravitational settings: the south-eastern Crati graben (Northern Calabria, Italy), *Tectonophysics, 396,* 181-193.

Tibaldi, A. (2001), Multiple sector collapses at Stromboli volcano, Italy: how they work, *Bull. Volcanol., 63,* 112-125.

Tibaldi, A., and G. Groppelli (2002), Volcano-tectonic activity along structures of the unstable NE flank of Mt. Etna (Italy) and their possible origin. *J. Volcanol. Geotherm. Res., 115,* 277-302.

Toutain, J.P., J.C. Baubron, J. Le Bronec, P. Allard, P. Briole, B. Marty, G. Miele, D. Tedesco and G. Luongo (1992), Continuous monitoring of distal gas emanations at Vulcano, southern Italy, *Bull. Volcanol., 54,* 147–155.

Toutain, J.P. and J.C. Baubron (1999), Gas geochemistry and seismotectonics: a review, *Tectonophysics, 304,* 1–27.

Voight, B. and D. Elsworth (1997), Failure of volcano slopes. *Geotechnique, 47,* 1-31.

Walter, T.R., V. Acocella, M. Neri and F. Amelung (2005), Feedback processes between magmatism and E-flank movement at Mt. Etna (Italy) during the 2002-2003 eruption. *J. Geophys. Res.,* 110, B10205, doi:10.1029/2005JB003688.

Figure captions

Figure 1 - Simplified geological map of Mt Etna showing the main structural features, including the three principal rift zones (NE, S and W) on the volcano and highlighting the unstable eastern and southern flanks as known before this study. The southern and eastern fronts of the spreading are evident from deformation of sediments on the southern margin of Etna and inferred from bathymetric data in the Ionian offshore (Borgia et al., 1992, 2000a, b). RFS = Ragalna fault system, MTFS = Mascalucia-Trecastagni fault system, PFS = Pernicana fault system, TFS = Timpe fault system, VB = Valle del Bove. Inset map: AI = Aeolian Islands, HP = Hyblean Plateau, ME = Malta Escarpment, MF = Messina fault system, ST = Sole thrust of the Appenine-Maghrebian Chain (rocks within the Chain are shown as Pre-Quaternary sedimentary rocks on the main map).

Figure 2 – EDM geodetic location map for stations across the central (N-S-striking) segment of the RFS. A: Geological map of the central region of the RFS taken from Rust and Neri (1996). See Figure 1 for location. Key: 1 = historical lavas, 2 = Recent Mongibello volcanics (< 8000 years), 3 = ignimbrites (about 14000 years), 4 = Ellittico autoclastic lava domes (34000-14000 years), 5 = Ellittico lavas (34000-14000 years), 6 = cinder cones, 7 = fault (bar on downthrown side, arrows indicate the lateral component of movement), 8 = drainage crossing the faults. B: Large scale topographic map showing the three geodetic stations used (see Map A for location). Contour interval = 10 m. See text for discussion.

Figure 3 –Durridge RAD7 instrument (A) used to measure radon concentrations in soils during surveys on Mt. Etna; see text for details. Sokkia SET3C Electronic Total Station instrument and EDM tripod (B) in position at Station 4, a prominent outcrop of massive lava, on the RFS; see Figure 2 for location.

Figure 4 – Left: the RFS projected onto a digital elevation model (DEM) of the south-western flank of Mt Etna. Known faults are shown as red lines (bars on downfaulted side); broken white lines are assumed fault segments (from Rust and Neri, 1996). Yellow lines indicate the positions of the five radon profiles discussed in the text. The box in the top left corner shows a contour map of radon (^{222}Rn) distribution (in bq m^{-3}) along the northern portion of the RFS; yellow circles identify radon measurement sites. Right: Graphs plotting radon (^{222}Rn) and thoron (^{220}Rn) emission, in bq m^{-3}, from soil along the five profiles. Grey vertical bar indicates the zones of highest radon values that can be associated with the presence of the fault.

Figure 5 – Time coverage of InSAR data. A) ERS-1 ERS-2 ascending pair 21 November 1993 – 30 September 1997. B) ERS-2 ERS-2 ascending pair 28 May 1997 – 13 May 1998. C) ERS-2 ERS-2 ascending pair 8 January 1997 – 8 March 2000. D) ERS-2 ERS-2 ascending pair 8 November 2000 – 9 October 2002.

Figure 6 - Phase interferograms of the study area (A = 21 November 1993 – 30 September 1997; B = 28 May 1997 – 13 May 1998) paired with their interpretation (A' and B') (see figure 1 for location). Numbers at the corners of each interferogram are the UTM coordinates in kilometers. LOS = Line Of Sight. Yellow lines represent previously known faults; broken white lines represent the presumed continuations of these faults. Black arrows indicate the faults that have moved in the period concerned, as deduced by InSAR data. Activity on the RFS is clearly recognizable throughout the period analyzed. In the

1993-1997 interval (interferograms A and A') the possible northern continuation (broken pink line) of the central N-S fault segment of RFS is clear. See text for discussion.

Figure 7 - Phase interferograms C (9 January 1997 – 8 March 2000) and D (8 November 2000 – 9 October 2002) and their paired interpretataions (C' and D'). Symbols as in Figure 6. Again, activity on the RFS is seen throughout the period. The possible northern continuation (broken pink line) of the central N-S fault segment of RFS is visible at least until 2000 (interferograms C and C'). During the final time interval analysed (interferograms D and D') the apparent north-eastern extension of the RFS connecting to the Etnean summit craters area is clearly displayed. See text for discussion.

Figure 8 – The Ragalna Fault System as deduced by the present study. In the left panel: ? = uncertainty in the continuity of faulting; red lines = known faults; broken orange lines = interpreted continuations of the main fault segment; yellow arrow = directon of movement in Block 3 (Neri et al, 2004). Other symbols as in Figures 1 and 6. See text for details.

Table captions

Table 1 - Raw ERS SAR data used.

Table 2 - EDM geodetic data for the N-S-striking central fault segment of the RFS (see Figure 2 for location) over a 6.5-year interval. Measurements were made using a Sokkia SET3C Electronic Total Station that outputs measurements digitally in fractions of a metre. Other distances are rounded to the nearest millimetre and rates to the nearest half millimetre. *****All measurements were repeated using the standard protocol of rotating the instrument on its tripod mount 180^{o} about both horizontal and vertical axes between measurements. **+**Corrections were made, using trigonometry, to allow for the 20^{o} angular difference between the geodetic lines and the strike of the fault; providing more accurate measurements for extensional (Station 1 – Station 3) and right-lateral strike-slip (Station 1 – Station 4) components of movement. See text for discussion.

SATELLITE	ORBIT	TRACK	FRAME	DATE	TIME
ERS1	*12298*	*129*	*747*	21/11/1993	*21:16*
ERS2	*09001*	*129*	*747*	08/01/1997	*21:16*
ERS2	*11005*	*129*	*747*	28/05/1997	*21:16*
ERS2	*12508*	*129*	*747*	10/09/1997	*21:16*
ERS2	*16015*	*129*	*747*	13/05/1998	*21:16*
ERS2	*25534*	*129*	*747*	08/03/2000	*21:16*
ERS2	*29041*	*129*	*747*	08/11/2000	*21:16*
ERS2	*39061*	*129*	*747*	09/10/2002	*21:16*

Table 1

Horizontal distance between Station 1 and Station 3	**1st measurement**	**2nd measurement***
11 Mar 1999 measurements	66.518 m	66.518 m
10 Nov 2005 measurements	66.541 m	66.543 m
Change in distance	23 mm increase	25 mm increase
Angularly corrected distance+ (equivalent to extension at right angles to the fault)	24 mm increase	27 mm increase
Average maximum rate for extensional component of movement for past 6.5 years	3.5 - 4 mm a^{-1}	

Horizontal distance between Station 1 and Station 4	**1st measurement**	**2nd measurement***
11 Mar 1999 measurements:	250.710 m	250.707 m
10 Nov 2005 measurements:	250.680 m	250.682 m
Change in distance	30 mm decrease	25 mm decrease
Angularly corrected distance+ (equivalent to right-lateral strike-slip movement parallel to the fault)	32 mm decrease	27 mm decrease
Average minimum rate for right-lateral strike-slip component of movement for past 6.5 years	4 – 5 mm a^{-1}	

Table 2

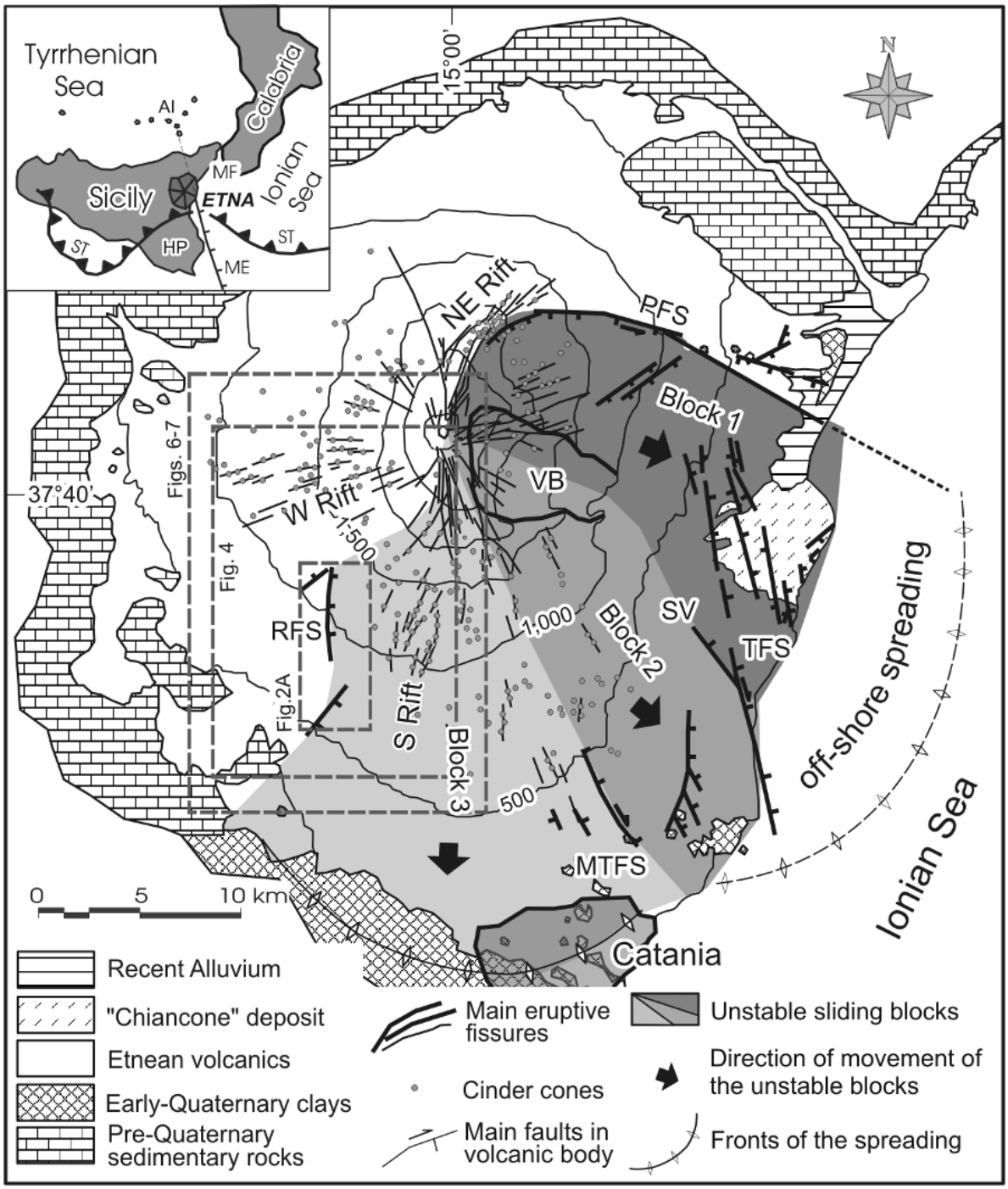
Tyrrhenian Sea
Calabria
AI
MF
Sicily
ETNA
Ionian Sea
ST
HP
ST
ME
15°00'
N
NE Rift
RFS
Block 1
VB
Figs. 6-7
37°40'
W Rift
1,500
Fig. 4
RFS
1,000
Block 2
SV
TFS
off-shore spreading
Fig.2A
S Rift
Block 3
500
MTFS
0 5 10 km
Ionian Sea
Catania
Recent Alluvium
"Chiancone" deposit
Etnean volcanics
Early-Quaternary clays
Pre-Quaternary sedimentary rocks
Main eruptive fissures
Cinder cones
Main faults in volcanic body
Unstable sliding blocks
Direction of movement of the unstable blocks
Fronts of the spreading

Figure 1

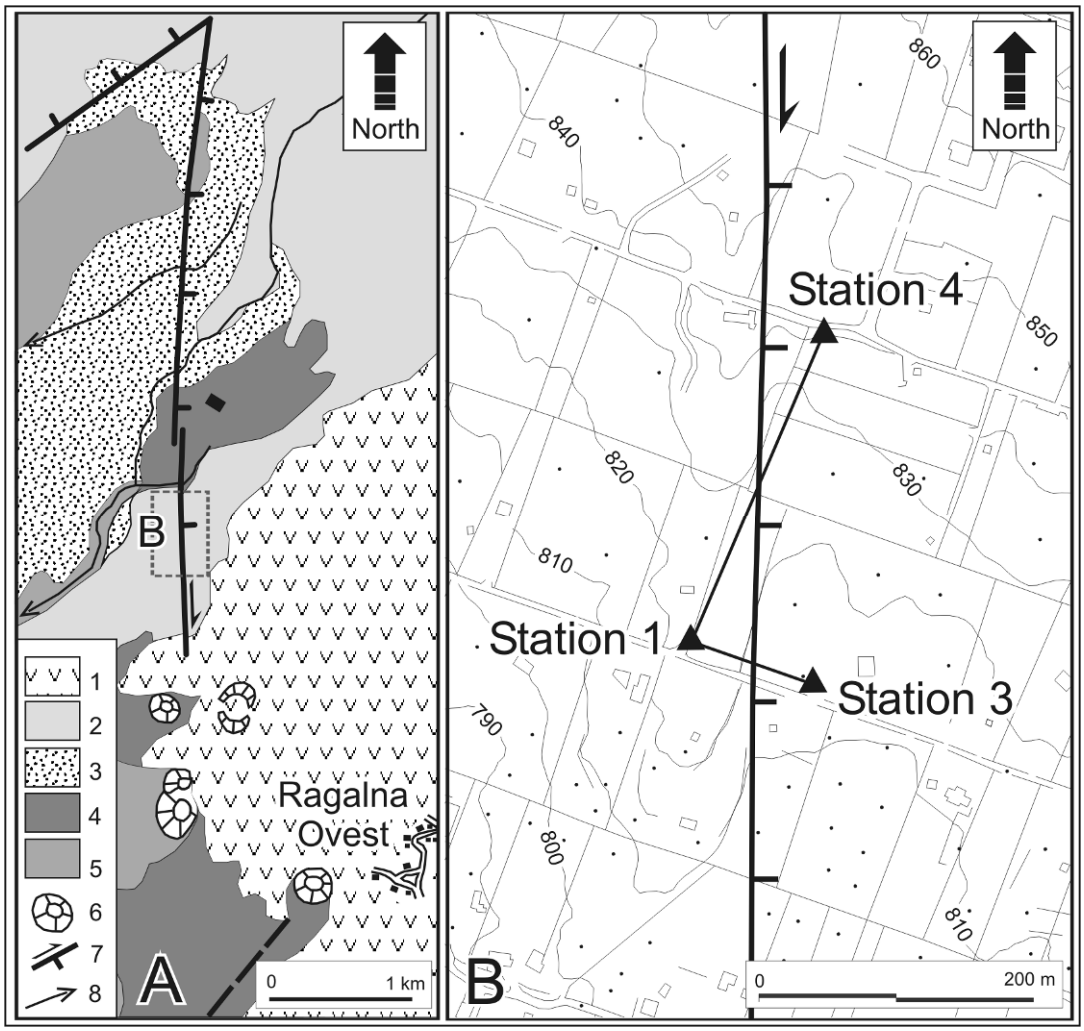
North
B
1
2
3
4
5
6
7
8
Ragalna
Ovest
A
0
1 km
B
North
860
840
850
820
830
810
790
800
810
Station 4
Station 1
Station 3
0
200 m

Figure 2

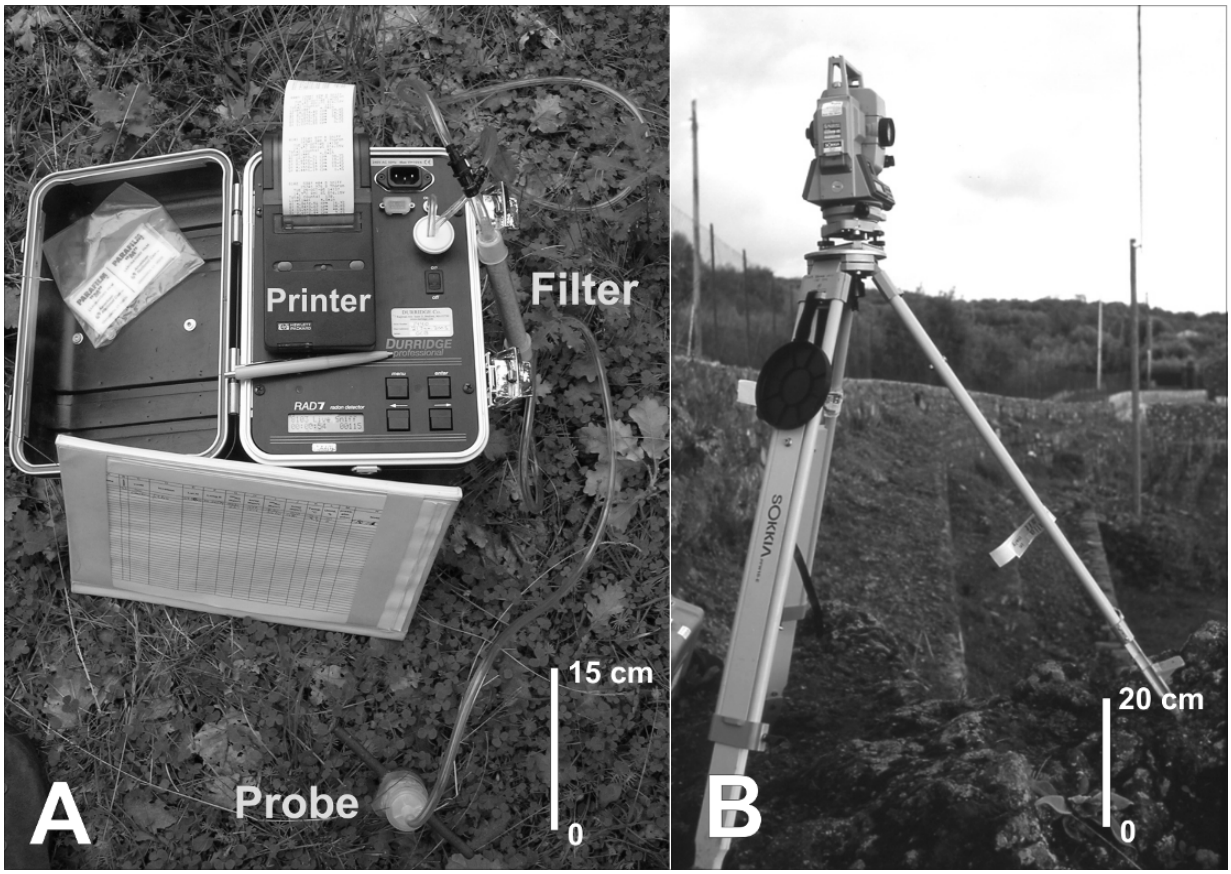
Printer
Filter
DURRIDGE
professional
RAD7
15 cm
0
A
Probe
SOKKIA
20 cm
0
B

Figure 3

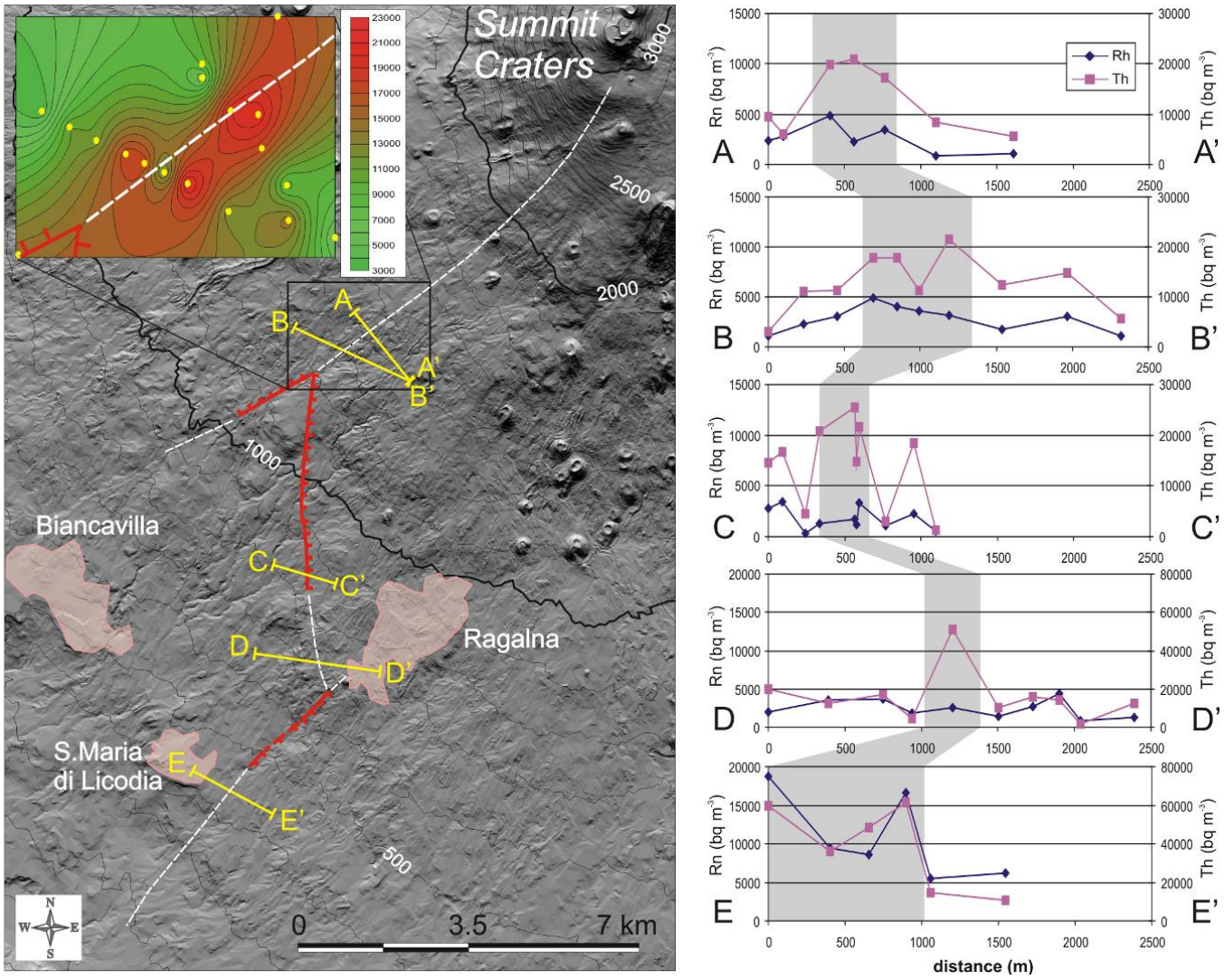
Summit Craters
3000
2500
2000
1000
500
Biancavilla
Ragalna
S.Maria di Licodia
A
A'
B
B'
C
C'
D
D'
E
E'
N
W
E
S
0
3.5
7 km
23000
21000
19000
17000
15000
13000
11000
9000
7000
5000
3000
Rn (bq m-3)
Th (bq m-3)
Rh
Th
distance (m)

Figure 4

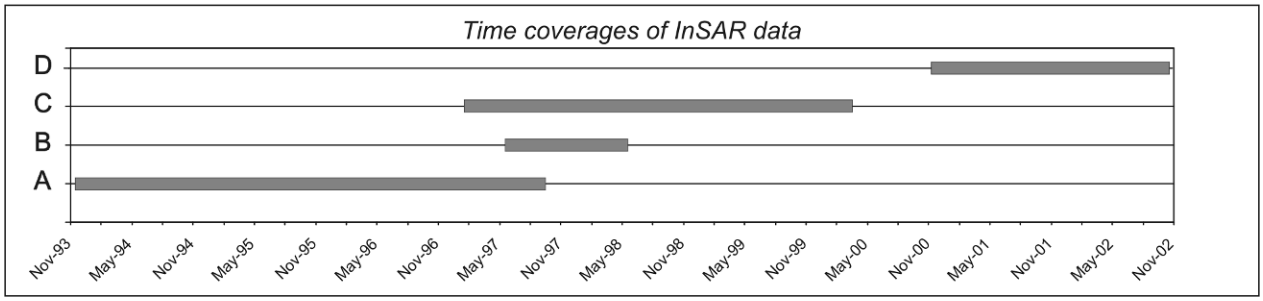

Figure 5

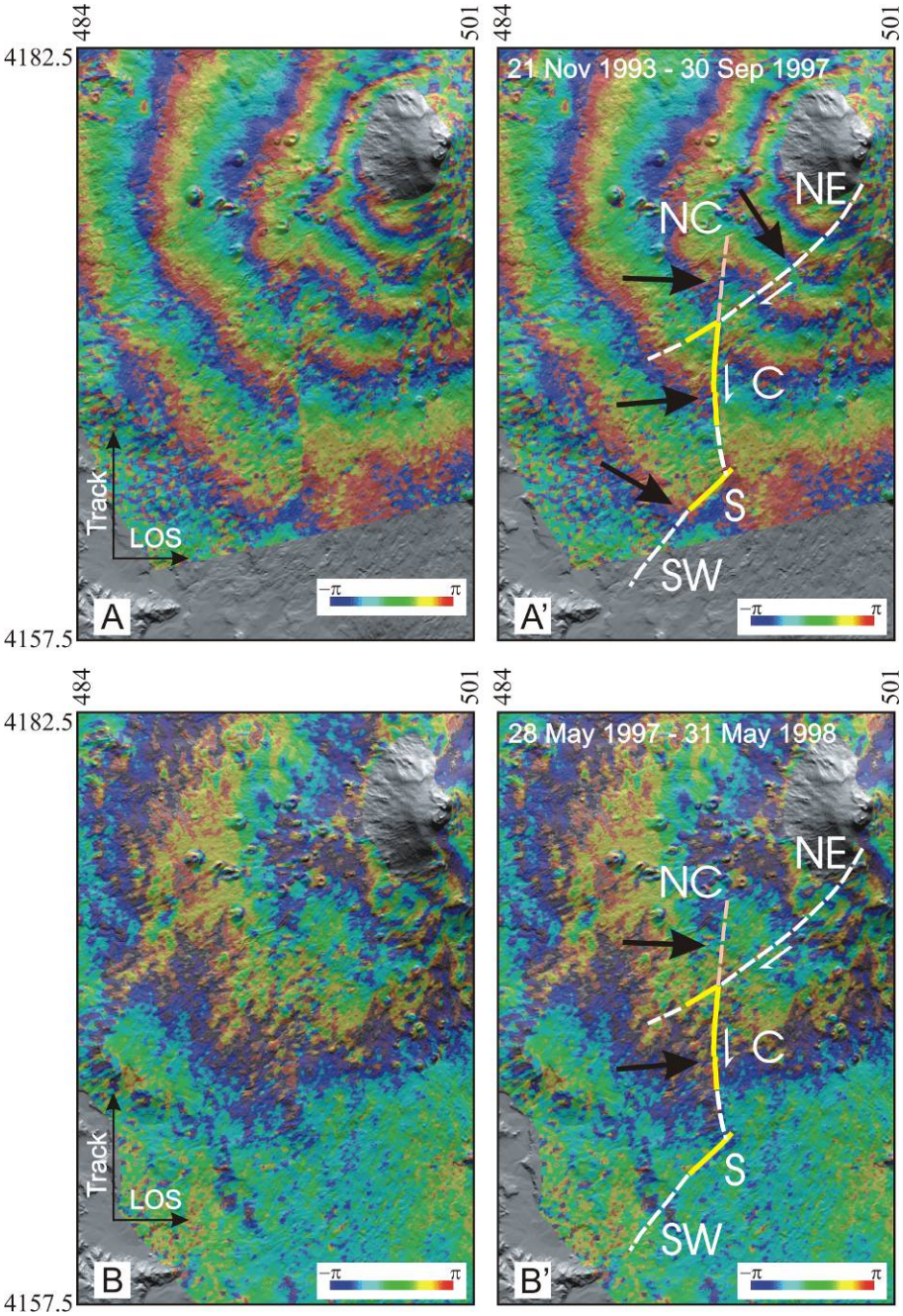

Figure 6

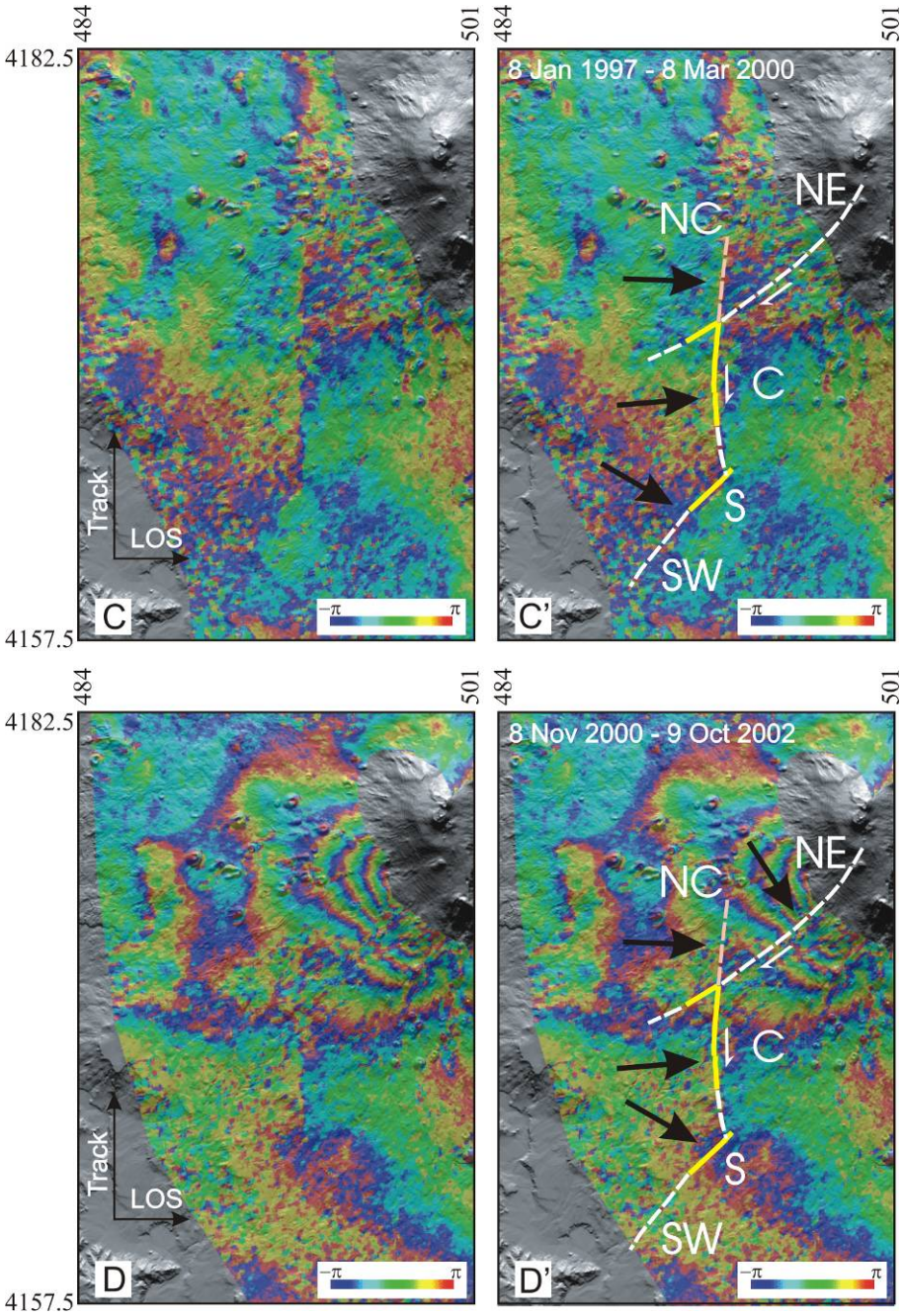
484
501
4182.5
4157.5
8 Jan 1997 - 8 Mar 2000
NC
NE
C
S
SW
Track
LOS
C
C'
8 Nov 2000 - 9 Oct 2002
D
D'
−π
π

Figure 7

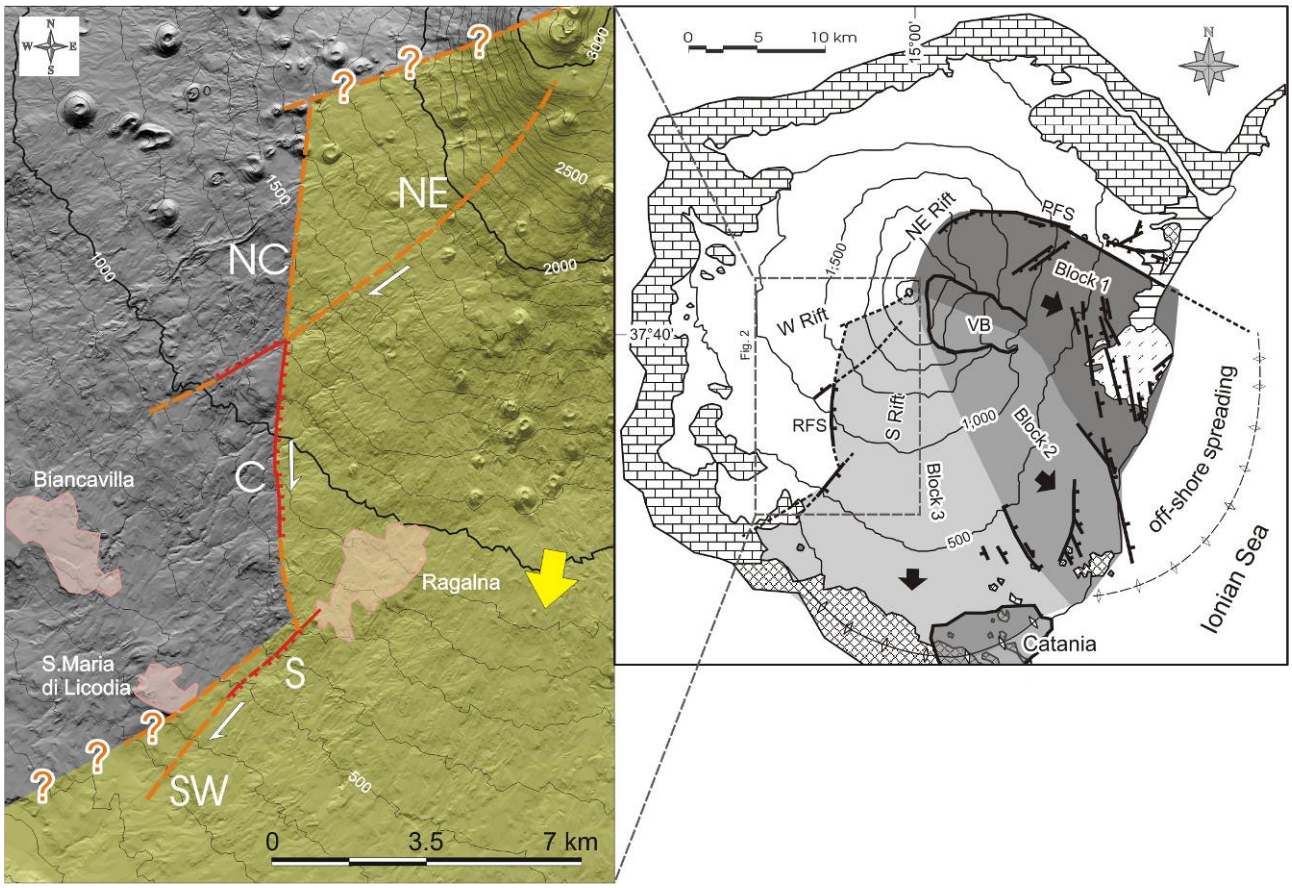
N
W
E
S
NE
NC
C
SW
Biancavilla
Ragalna
S.Maria
di Licodia
3000
2500
2000
1500
1000
500
0
3.5
7 km
0
5
10 km
15°00'
37°40'
Fig. 2
NE Rift
RFS
W Rift
VB
S Rift
Block 1
Block 2
Block 3
off-shore spreading
Ionian Sea
Catania

Figure 8